Astronomy & Astrophysics manuscript no. output
April 27, 2026

Dynamical properties and star formation history of a low-mass quenched galaxy at cosmic noon

K. Ito[1,2], F. Valentino[1,2], W. M. Baker[3], G. Brammer[1,4], R. Gottumukkala[1,4], T. Kakimoto[5,6], C. D. P. Lagos[7,8,1], M. Onodera[5,9], A. Pensabene[1,2], G. Scarpe[1,2], M. Tanaka[5,6], K. E. Whitaker[10,1], N. A. Reddy[11], R. L. Sanders[12], and A. E. Shapley[13]

[1] Cosmic Dawn Center (DAWN), Copenhagen, Denmark
[2] DTU Space, Technical University of Denmark, Elektrovej 327, DK2800 Kgs. Lyngby, Denmark
[3] DARK, Niels Bohr Institute, University of Copenhagen, Jagtvej 155A, DK-2200 Copenhagen, Denmark
[4] Niels Bohr Institute, University of Copenhagen, Jagtvej 128, 2200 Copenhagen N, Denmark
[5] Department of Astronomical Science, The Graduate University for Advanced Studies, SOKENDAI, 2-21-1 Osawa, Mitaka, Tokyo 181-8588, Japan
[6] National Astronomical Observatory of Japan, 2-21-1 Osawa, Mitaka, Tokyo 181-8588, Japan
[7] International Centre for Radio Astronomy Research (ICRAR), M468, University of Western Australia, 35 Stirling Hwy, Crawley, WA 6009, Australia
[8] ARC Centre of Excellence for All Sky Astrophysics in 3 Dimensions (ASTRO 3D)
[9] Subaru Telescope, National Astronomical Observatory of Japan, National Institutes of Natural Sciences (NINS), 650 North A'ohoku Place, Hilo, HI 96720, USA
[10] Department of Astronomy, University of Massachusetts, Amherst, MA 01003, USA
[11] Department of Physics & Astronomy, University of California, Riverside, 900 University Avenue, Riverside, CA 92521, USA
[12] Department of Physics and Astronomy, University of Kentucky, 505 Rose Street, Lexington, KY 40506, USA
[13] Department of Physics & Astronomy, University of California, Los Angeles, 430 Portola Plaza, Los Angeles, CA 90095, USA

Received -, Accepted -

ABSTRACT

We present the spectroscopic confirmation and in-depth analysis of AURORA-LQG1, a low-mass quiescent galaxy at $z_{\rm spec} = 2.0834$ with $\log(M_\star/M_\odot) = 9.6$, observed with medium-resolution JWST/NIRSpec spectroscopy. Its stellar mass places approximately ten times lower than the knee of the stellar mass function for quiescent galaxies at $z \sim 2$. The deep medium-resolution spectrum enables the measurement of its stellar velocity dispersion ($\sigma_\star = 95^{+38}_{-33}$ km s^{-1}), the smallest value recorded among spectroscopically confirmed quiescent galaxies at $z \sim 2$. Coupled with a compact size (0.41 ± 0.03 kpc in the rest-frame optical), the stellar velocity dispersion yields a dynamical mass estimate of $\log(M_{\rm dyn}/M_\odot) = 9.75^{+0.29}_{-0.38}$, consistent with the stellar mass, confirming the true low-mass nature of this galaxy and placing a first constraint on its initial mass function. Joint spectro-photometric spectral energy distribution fitting reveals a star formation history in which half the stellar mass was in place ~ 1 Gyr before the observed epoch, with quenching occurring ~ 0.2 Gyr prior to $z = 2.08$. These results confirm that AURORA-LQG1 is genuinely quenched, rather than in a temporary phase of suppressed star formation. AURORA-LQG1 is consistent with the mass fundamental plane at $z \sim 2$, which was previously constrained only by massive quiescent systems with $M_\star \geq 10^{11}\,M_\odot$ at cosmic noon. Compared with more massive counterparts at the same epoch observed with similar NIRSpec grating spectroscopy, the time since quenching for AURORA-LQG1 is among the shortest observed. The star formation history of AURORA-LQG1 is broadly consistent with predictions for quiescent galaxies of similar mass and redshift in the IllustrisTNG and SHARK models. The galaxy resides in a possible dense group-scale (~ 50 kpc) environment containing one companion with tentative spectroscopic redshift and five low-mass companion candidates with similar redshifts, and it is embedded in a large known protocluster on megaparsec scales. A potential environmental influence on its evolution could explain the outside-in quenching suggested by the positive gradient of size with wavelength. This study demonstrates that deep JWST/NIRSpec spectroscopy enables low-mass quiescent galaxies at cosmic noon to be characterized with a level of detail long reserved for massive systems, offering valuable new insights into how quenching operates in these underexplored, low-mass systems.

Key words. galaxies: evolution - galaxies: high-redshift - galaxies: stellar content - galaxies: elliptical and lenticular, cD

1. Introduction

It is well known that mass and environment correlate with galaxy quenching in the local Universe, reflecting a wide range of physical mechanisms and timescales involved (Peng et al. 2010). Internal "ejective" processes – such as gas outflows driven by active galactic nuclei (AGNs) or supernovae (SNe) – can shut down star formation rapidly on $< 0.1 - 0.5$ Gyr timescales (e.g., Croton et al. 2006; Fabian 2012), whereas "preventive" mechanisms such as morphological stabilization act more slowly ($\gtrsim 1$ Gyr). Low-mass galaxies are additionally susceptible to external processes: ram-pressure stripping can quench them on similarly short timescales ($< 0.1 - 0.5$ Gyr; Gunn & Gott 1972), while starvation operates more gradually over $\sim 1 - 5$ Gyr in dense environments (Peng et al. 2015; Cortese et al. 2021).

Much of our current knowledge of how star formation ceases in galaxies at high redshift comes from massive objects, whose quenching is thought to be dominated by internal mechanisms and can be probed with high-quality near-infrared (NIR) spec-

Article published by EDP Sciences, to be cited as https://doi.org/10.1051/0004-6361/202558795

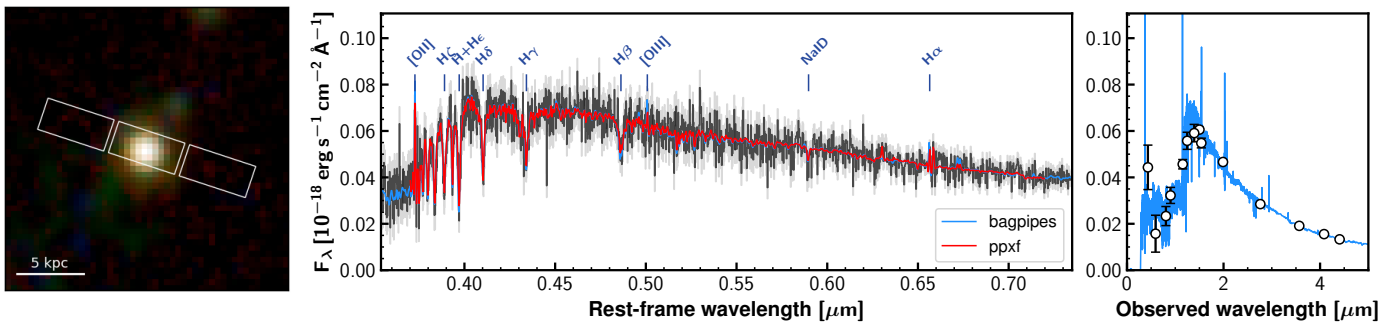

Fig. 1: Left panel: 2″ × 2″ JWST/NIRCam composite image of AURORA-LQG1. Images taken with the F115W, F150W, and F444W filters are used as the blue, green, and red channels. The white boxes indicate the NIRSpec/MSA slitlet positioning. Middle panel: JWST/NIRSpec spectrum of AURORA-LQG1. The black line and gray-shaded region correspond to the observed spectrum and its 1σ uncertainty, respectively. The red and blue lines correspond to the best-fit from pPXF (Sect. 3.1) and Bagpipes (Sect. 3.2), respectively. Right panel: Photometric SED of AURORA-LQG1. The blue line represents the best-fit SED obtained with Bagpipes.

troscopy. Over the past decade, spectroscopic observations have confirmed a substantial population of red, quiescent galaxies at early times (e.g., Cimatti et al. 2004; Glazebrook et al. 2017; Schreiber et al. 2018; Tanaka et al. 2019; Valentino et al. 2020; Forrest et al. 2020; Esdaile et al. 2021; Kakimoto et al. 2024). This effort has been transformed by JWST: its exceptional sensitivity enables clear detections of stellar continua in massive quiescent galaxies ($\log(M_\star/M_\odot) > 10$) at $z \sim 2-7$, with absorption features and overall spectral shapes yielding robust measurements of their star formation histories, stellar velocity dispersions, chemical compositions, and surrounding environments (e.g., Marchesini et al. 2023; Belli et al. 2024; Davies et al. 2024; Wu 2025; Antwi-Danso et al. 2025; Beverage et al. 2024; Carnall et al. 2024; Glazebrook et al. 2024; Slob et al. 2024; Nanayakkara et al. 2025; de Graaff et al. 2025b; Weibel et al. 2025; Valentino et al. 2025; Baker et al. 2025b, 2026; McConachie et al. 2025; Ito et al. 2025a; Slob et al. 2025).

Photometric studies, especially those using deep JWST imaging, have also established the presence of a population of quiescent galaxies extending to much lower stellar masses, revealing their abundance and morphological properties (Weaver et al. 2023; Cutler et al. 2024; Alberts et al. 2024; Baker et al. 2025c; Shuntov et al. 2026; Hamadouche et al. 2025). The resulting stellar mass functions (SMFs) rise from high masses to a peak around $M_\star \sim 10^{10.5}\,M_\odot$ at $z \sim 2$, while at lower masses the mechanisms traditionally associated with the onset of environmental effects progressively build up the power-law tail of the classical Schechter function. Stellar masses even 1 dex below the SMF peak of quiescent galaxies at $z \sim 2$ hold the promise of constraining such environmental effects and are becoming key to calibrating simulations and models (Lagos et al. 2025; Baker et al. 2025c; Shuntov et al. 2026). Nevertheless, this mass range is almost unexplored spectroscopically. Moreover, the rare spectroscopic confirmations of quiescent galaxies with $\log(M_\star/M_\odot) < 10$ at $z \gtrsim 2$ rely on low-resolution spectroscopy (NIRSpec/PRISM or grism observations; Sandles et al. 2023; Sato et al. 2024; Baker et al. 2025b, 2026), largely because of the long integration times required. This severely limits the physical analysis of the formation and evolution of these systems compared with the level of detail attained for their more massive counterparts, and it completely prevents a first assessment of their dynamical properties.

This paper reports the characterization of a low-mass quiescent galaxy, AURORA-LQG1, with $\log(M_\star/M_\odot) = 9.6$ at $z = 2.08$, about ten times less massive than the SMF peak of quiescent galaxies at this redshift (e.g., Weaver et al. 2023). The analysis is based on deep JWST/NIRSpec medium-resolution spectroscopy combined with JWST/NIRCam and HST imaging. The medium spectral resolution is crucial for confirming the low-mass nature of this system through a first estimate of its dynamical mass and a robust spectrophotometric modeling of its star formation history, achieving a level of quality comparable to that obtained for more massive counterparts. At lower redshifts, less massive galaxies are known to have formed more recently than their massive counterparts, a phenomenon referred to as "downsizing" (Thomas et al. 2005, 2010; Gallazzi et al. 2005, 2025). Observations and analyses of low-mass quiescent galaxies such as that presented here thus provide an ideal opportunity to explore the mass dependence of star formation histories at cosmic noon, in light of results for massive systems in the literature (e.g., Park et al. 2024; Baker et al. 2025b; Nanayakkara et al. 2025).

This work is structured as follows. Section 2 summarizes the dataset used in this paper. In Sect. 3, we present the spectral analysis, deriving the kinematical (Sect. 3.1) and stellar population properties (Sect. 3.2). Section 4 compares the dynamical properties with well-established scaling relations. In Sect. 5, we discuss the dependence of the star formation history on stellar mass and the group-like environment surrounding our target. Throughout our study, we use the AB magnitude system (Oke & Gunn 1983). We adopt a Λ cold dark matter cosmology with $\Omega_m = 0.3$, $\Omega_\Lambda = 0.7$, and $H_0 = 70\,\mathrm{km\,s^{-1}\,Mpc^{-1}}$.

2. Target selection and data

We selected our target galaxy, AURORA-LQG1 (Fig. 1), as part of the DeepDive program and archival search for quiescent galaxies with NIRSpec/Micro-shatter array (MSA) medium- or high-resolution spectroscopy at high redshift (Ito et al. 2025a). AURORA-LQG1 is in the COSMOS field (Scoville et al. 2007). It was selected based on its high D_n4000 value ($D_n4000 = 1.35 \pm 0.03$, defined as in Balogh et al. 1999), its UVJ rest-frame colors ($U - V = 1.18 \pm 0.09$, $V - J = 0.63 \pm 0.06$), falling within the selection box of Williams et al. (2009) with a 0.2 dex margin, and its low specific star formation rate (sSFR) from photometric spectral energy distribution (SED) fitting. This places the galaxy more than one dex below the star-formation main sequence in Schreiber et al. (2015). We briefly summarize the data available for AURORA-LQG1 and the reduction below, and we refer the reader to Ito et al. (2025a) and references therein for all details.

We retrieved JWST/NIRCam and HST imaging data (v7) from the Dawn JWST Archive (DJA)[1]. JWST/NIRCam data were obtained as part of the Public Release IMaging for Extragalactic Research (PRIMER) Survey (PID #1837; PI: Dunlop) and reduced with Grizli (Brammer 2023a; Valentino et al. 2023). We used photometry measured in circular apertures with a diameter of 0.″5 and corrected to "total" values within Kron apertures (Kron 1980), which were computed on the detection image obtained by combining filters in the long-wavelength channels. We used imaging obtained with the F090W, F115W, F150W, F200W, F277W, F356W, F410M, and F444W filters from JWST/NIRCam, as well as the F814W, F125W, F140W, and F160W bands from HST/ACS and WFC3.

JWST/NIRSpec spectroscopic data of AURORA-LQG1 were collected as a part of the Assembly of Ultradeep Rest-optical Observations Revealing Astrophysics program[2] (AURORA, PID #1914, Co-PIs: A. Shapley and R. Sanders, Shapley et al. 2025). Spectra were collected with the G140M/F100LP, G235M/F170LP, and G395M/F290LP combinations, with exposure times of 44,204s, 28,886s, and 15,056s, respectively. Here we focus on the G140M/F100LP and G235M/F170LP spectra mapping the rest-frame optical wavelengths at $z = 2$. The data were reduced using the Msaexp software (Brammer 2023b; Heintz et al. 2025; de Graaff et al. 2025a). The latest version of the reduction available on DJA (v4[3], Valentino et al. 2025) extends the wavelength coverage of each spectrum. Once optimally extracted (Horne 1986), we calibrated the spectra against flux losses and contamination from higher-order spectra with a custom correction for quiescent galaxies (Ito et al. 2025a). The flux-loss calibration was applied by anchoring the observed spectra to the total photometry with a second-order polynomial. The spectra and SED of AURORA-LQG1 are shown in Fig. 1. Although the galaxy is faint ($m_{\rm F150W} = 24.8$ mag), the 12-hour spectrum achieves a signal-to-noise ratio of 12 per pixel in the rest-frame interval $0.4\,\mu{\rm m} < \lambda_{\rm rest} < 0.5\,\mu{\rm m}$.

3. Spectral analysis

3.1. Redshift and stellar velocity dispersion

We conducted stellar template fitting using the penalized pixel-fitting algorithm (pPXF, Cappellari 2017, 2023) and derived the redshift and stellar velocity dispersion ($\sigma_\star$) of AURORA-LQG1. We adopted the flexible stellar population synthesis (FSPS) models (Conroy & Gunn 2010) with MILES stellar libraries (Sánchez-Blázquez et al. 2006; Falcón-Barroso et al. 2011) as templates. We allowed the stellar ages to be younger than the age of the Universe at the redshift of the target and the metallicities to range between [M/H] = −2 and 0.5.

A careful treatment of the NIRSpec instrumental resolution is essential for an accurate stellar velocity dispersion measurement. Recent work has shown that the in-flight spectral resolution is higher than the pre-launch estimates (de Graaff et al. 2024). Here we adopted the JDox resolution curve[4] scaled up by a factor of 1.3 (de Graaff et al. 2025b; Valentino et al. 2025). This factor is consistent with the prescription of Slob et al. (2024) for sources of size comparable to AURORA-LQG1 (Sect. 4.1). Although the exact correction also depends mildly on source position, the resulting variation is at the ∼ 10% level and does not affect our analysis. The wavelength-dependent resolution curve was incorporated into pPXF, and the templates were convolved accordingly.

Following previous studies (e.g., Scholz-Díaz et al. 2022), we derived the kinematical and stellar population properties using a two-step process. Both steps were performed over the wavelength range $0.37\,\mu{\rm m} < \lambda < 0.72\,\mu{\rm m}$ due to the resolution of the MILES templates. In the first step, we constrained the stellar kinematics by estimating the velocity offset (i.e., a refined redshift) and the stellar velocity dispersion. To mitigate potential mismatches between the observed spectrum and the stellar templates, we flattened both by modeling the spectral shape with a third-order B-spline function and dividing the spectra by this function prior to fitting. During this step of the pPXF fitting, we modeled only the stellar continuum and masked strong emission lines (Hα, [N II], [O III], Hβ, and [O II]), as well as the sodium absorption doublet (NaI D). The latter may be possibly affected by absorption from the neutral interstellar gas and outflows, commonly observed at $z \sim 2$ (Davies et al. 2024). A second-order additive polynomial correction was also included. This step was iterated 1000 times by adding random noise to the observed spectra to estimate the uncertainties on z and $\sigma_\star$. In the second step, we reran ppxf, simultaneously modeling the stellar continuum and emission lines while fixing the kinematics to the values obtained in the first step. A second-order multiplicative polynomial correction was included this time, and the NaI D absorption was again masked. This second step was also iterated 1000 times to estimate the uncertainties on the stellar population properties, such as stellar age and metallicity, as well as on emission line fluxes.

Figure 1 shows the best-fit model from pPXF. The best-fit redshift is $z_{\rm spec} = 2.0834^{+0.0002}_{-0.0002}$, used hereafter. We estimate a stellar velocity dispersion of $\sigma_\star = 95^{+38}_{-33}\,{\rm km\,s^{-1}}$, which is the lowest stellar velocity dispersion reported so far at $z \geq 2$ (e.g., Belli et al. 2014, 2017; Tanaka et al. 2019; Stockmann et al. 2020; Esdaile et al. 2021; Forrest et al. 2022; Slob et al. 2025). Appendix A shows the probability distribution of the measured stellar velocity dispersion. The measured emission line fluxes are also summarized in Table 1. The Hα line is detected at a significance of 7σ, allowing us to estimate the instantaneous star formation rate (SFR) following Kennicutt & Evans (2012), assuming a negligible contribution from AGNs. This assumption is supported by the [O III]/Hβ and [N II]/Hα ratios, which, despite their large uncertainties ($\log([{\rm OIII}]\lambda5007/{\rm H}\beta) = -0.22^{+0.21}_{-0.29}$ and $\log([{\rm NII}]\lambda6583/{\rm H}\alpha) = -0.26^{+0.11}_{-0.13}$, respectively), suggest no significant AGN contribution according to the Baldwin, Phillips & Terlevich diagnostic diagram (Kewley et al. 2013). Given the large uncertainties on the Hβ line flux and the negligible dust extinction on the stellar continuum inferred from the SED fitting (see Sect. 3.2), we did not apply dust-attenuation correction to the line fluxes. The resulting instantaneous SFR is ${\rm SFR}_{\rm H\alpha} = 0.08^{+0.01}_{-0.01}\,M_\odot\,{\rm yr^{-1}}$.

3.2. SED modeling

We used Bagpipes (Carnall et al. 2018, 2019b) to model the spectra at $0.35\,\mu{\rm m} < \lambda < 0.74\,\mu{\rm m}$ and photometry simultaneously. We adopted the stellar population models from Bruzual & Charlot (2003), with the MILES stellar spectral library and stellar evolutionary tracks from Bressan et al. (2012),

[1] https://dawn-cph.github.io/dja/
[2] The ID of this galaxy in the AURORA survey is 4631.
[3] https://doi.org/10.5281/zenodo.15472354
[4] https://jwst-docs.stsci.edu/jwst-near-infrared-spectrograph/nirspec-instrumentation/nirspec-dispersers-and-filters#gsc.tab=0

assuming the initial mass function (IMF) from Kroupa (2001), the dust attenuation law from Calzetti et al. (2000), and the grid of nebular emission lines with a constant ionization parameter $\log U = -3$. We assumed two different star formation histories: a double power-law function (Carnall et al. 2019a) and a nonparametric continuity model (Leja et al. 2019). In addition to the star formation history, the stellar metallicity and velocity dispersion were set as free parameters. The redshift was fixed to the spectroscopic estimate from pPXF. We also included a second-order polynomial function in the fit to correct the mismatch between the stellar templates and spectra as well as an extra white noise scaling factor. The effect of the varying resolution in JWST grating spectra was accounted for by inputting the resolution curve described above. Consistent with our approach to model the spectrum with pPXF, we masked out the spectrum around the Hα, [N II], [O III], Hβ, and [O II] emission lines and the NaI D absorption feature. Priors and the allowed range of free parameters are summarized in Appendix B.

We report the best-fit parameters in Table 1. The best-fit models of the spectra and the photometry are shown in Fig. 1. With a double power-law parameterization of the star formation history (SFH), we obtain a stellar mass of $\log(M_\star/M_\odot) = 9.612^{+0.009}_{-0.012}$ and a SFR averaged over 100 Myr of SFR $= 0.14^{+0.03}_{-0.03}\,M_\odot\,\mathrm{yr}^{-1}$. The error bars on $M_\star$ reflect the statistical uncertainties of the fitting process, while systematic uncertainties of ~ 0.2 dex are known to affect this parameter's estimate (Pacifici et al. 2023). Although the timescale of interest is different, the SFR from the SED modeling is broadly consistent with the instantaneous SFR from Hα ($\mathrm{SFR}_{\mathrm{H}\alpha} = 0.08^{+0.01}_{-0.01}\,M_\odot\,\mathrm{yr}^{-1}$; see Sect. 3.1). This corresponds to an sSFR being 1 dex lower than for main-sequence galaxies with the same stellar mass at $z = 2$ (e.g., Schreiber et al. 2015; Popesso et al. 2023), and lower than $0.2/t_{\mathrm{age}}$, where t_{age} is the age of the Universe at that redshift. This makes AURORA-LQG1 one of the least massive quiescent galaxies at $z \geq 2$ observed with NIRSpec grating spectra (for those observed with PRISM spectra, see Baker et al. 2025b; Sandles et al. 2023; Sato et al. 2024; Baker et al. 2026). We obtain consistent results with the nonparametric SFH (Table 1). The stellar velocity dispersion derived from Bagpipes is consistent with that from pPXF.

3.3. Star formation history and metal enrichment

Figure 2 shows the SFH of AURORA-LQG1 derived from spectro-photometric modeling using Bagpipes. The double power-law and nonparametric models show similar shapes overall. The formation time, i.e., the time after the Big Bang when half of the observed stellar mass formed, are $t_{\mathrm{form}} = 2.33^{+0.03}_{-0.06}$ Gyr and $t_{\mathrm{form}} = 2.14^{+0.09}_{-0.13}$ Gyr for the double power-law model and the nonparametric model, respectively. This formation time means that the half of the stellar mass of AURORA-LQG1formed $\sim$ 1 Gyr before the observed redshift, consistent with the stellar age estimate from the pPXF fitting ($1.55^{+0.31}_{-0.34}$ Gyr). We also computed the quenching time, defined as the epoch when sSFR $\leq 0.2/t_{\mathrm{age}}$ after the formation time (e.g., Park et al. 2024; Baker et al. 2025b). Also, in this case, we find that both SFH parameterizations return similar quenching times ($2.91^{+0.02}_{-0.02}$ Gyr and $2.98^{+0.04}_{-0.06}$ Gyr after the Big Bang for the double power-law and the nonparametric models, respectively). The shape of the spectra and the ensuing formation and quenching timescales are thus similar to those of more massive quiescent galaxies (Park et al. 2024; Slob et al. 2024; Nanayakkara et al. 2024; Carnall et al. 2023, 2024). On the other hand, this low-mass galaxy is markedly different from those of lower-mass, bluer galaxies likely in a transitory phase of suppressed star formation (i.e., "mini-quenched" systems; Strait et al. 2023; Looser et al. 2024; Baker et al. 2025a). These "napping" systems typically are in the quenched phase on timescales of just tens of megayears (e.g., 40 Myrs as the stellar age of MACS0417-z5BBG, Strait et al. 2023), in contrast with the much older age of AURORA-LQG1. In Sect. 5.1, we compare in more detail the modeled SFHs with those of other massive quiescent galaxies at similar redshifts and in a cosmological simulation.

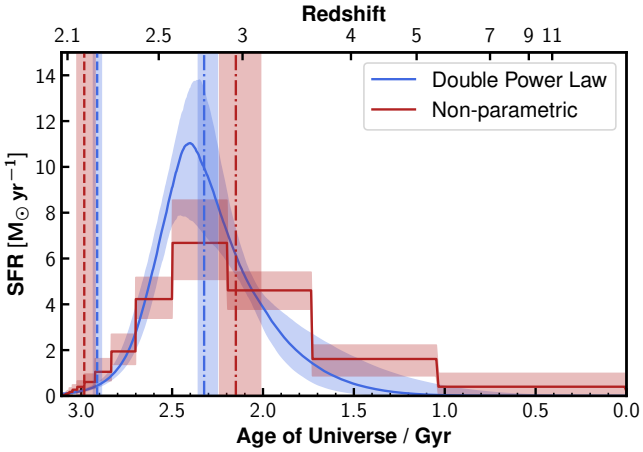

Fig. 2: Star formation history of AURORA-LQG1. The solid lines and shaded regions in blue and red indicate the medians and 16-84% ranges obtained by modeling the spectra and photometry with Bagpipes, assuming double power-law and nonparametric models, respectively. The vertical dashed-dotted and dashed lines in each color correspond to the formation and quenching times of the respective SFH models.

Modeling with Bagpipes yields stellar metallicities of $[\mathrm{M/H}] = 0.06^{+0.04}_{-0.06}$ and $[\mathrm{M/H}] = -0.07^{+0.04}_{-0.06}$ for the double power-law and nonparametric SFH models, respectively. These values are $\sim 0.3 - 0.4$ dex higher than the metallicity derived with pPXF ($[\mathrm{M/H}] = -0.41^{+0.22}_{-0.25}$). This discrepancy may arise from the different assumptions about the star formation history (de Graaff et al. 2025b) or from differences in the datasets used for modeling. In particular, both photometry and spectroscopy were included when running Bagpipes, whereas only the spectrum was used with pPXF. The limited sensitivity to weak metal absorption features was imprinted on the large uncertainty of the metallicity measurements, such that all three estimates are broadly consistent with the stellar metallicities of quiescent galaxies at similar stellar mass in the local Universe ($[\mathrm{M/H}] \sim -0.5$ with a 1σ scatter of 0.5 dex; Gallazzi et al. 2005; Mattolini et al. 2025; Gallazzi et al. 2025). This suggests that AURORA-LQG1 was already significantly metal-enriched by $z \sim 2$, reaching levels comparable to those of local quiescent galaxies, in agreement with studies of massive quiescent systems at similar redshift (Beverage et al. 2025).

4. Dynamical properties

4.1. Morphologies, sizes, and their gradients

We modeled the surface brightness of AURORA-LQG1 in the available JWST/NIRCam images taken with the F115W,

Table 1: Summary of the physical properties of AURORA-LQG1.

Parameter	Value
R.A.	150.156402
Decl.	2.224525
From pPXF[a]	
z	$2.0834^{+0.0002}_{-0.0002}$
$\sigma_\star$ [km s^{-1}]	95^{+38}_{-33}
[M/H]	$-0.41^{+0.22}_{-0.25}$
$t_{\rm age}$ [Gyr]	$1.55^{+0.31}_{-0.34}$
$f_{\rm H\beta}$ [erg s^{-1} cm^{-2}]	$2.4^{+0.7}_{-0.7} \times 10^{-19}$
$f_{\rm H\alpha}$ [erg s^{-1} cm^{-2}]	$5.0^{+0.7}_{-0.7} \times 10^{-19}$
$f_{\rm [OII]3726}$ [erg s^{-1} cm^{-2}]	$4.3^{+0.9}_{-1.0} \times 10^{-19}$
$f_{\rm [OII]3729}$ [erg s^{-1} cm^{-2}]	$1.9^{+0.9}_{-0.9} \times 10^{-19}$
$f_{\rm [OIII]}$ [erg s^{-1} cm^{-2}][b]	$2.2^{+0.9}_{-0.9} \times 10^{-19}$
$f_{\rm [OI]}$ [erg s^{-1} cm^{-2}]	$2.1^{+1.0}_{-1.0} \times 10^{-19}$
$f_{\rm [NII]}$ [erg s^{-1} cm^{-2}][b]	$3.5^{+0.8}_{-0.8} \times 10^{-19}$
SFR$_{\rm H\alpha}$ [$M_\odot$ yr^{-1}]	$0.08^{+0.01}_{-0.01}$
From Bagpipes with DPL SFH	
$\log(M_\star/M_\odot)$	$9.612^{+0.012}_{-0.009}$
SFR [$M_\odot$ yr^{-1}]	$0.14^{+0.03}_{-0.03}$
sSFR [yr^{-1}]	$3.4^{+0.7}_{-0.6} \times 10^{-11}$
A_V [mag]	$0.02^{+0.03}_{-0.01}$
[M/H]	$0.06^{+0.04}_{-0.06}$
$t_{\rm form}$[c] [Gyr]	$2.33^{+0.03}_{-0.06}$
$t_{\rm quench}$[c] [Gyr]	$2.91^{+0.02}_{-0.02}$
From Bagpipes with Nonparametric SFH	
$\log(M_\star/M_\odot)$	$9.630^{+0.013}_{-0.010}$
SFR [$M_\odot$ yr^{-1}]	$0.24^{+0.11}_{-0.10}$
sSFR [yr^{-1}]	$5.7^{+2.6}_{-2.5} \times 10^{-11}$
A_V [mag]	$0.03^{+0.03}_{-0.02}$
[M/H]	$-0.07^{+0.04}_{-0.06}$
$t_{\rm form}$[c] [Gyr]	$2.14^{+0.09}_{-0.13}$
$t_{\rm quench}$[c] [Gyr]	$2.98^{+0.04}_{-0.06}$
Morphological fitting in F150W	
R_e[d] [kpc]	$0.41^{+0.03}_{-0.03}$
n	$3.04^{+0.52}_{-0.45}$
q[e]	$0.85^{+0.08}_{-0.06}$
$\log(M_{\rm dyn}/M_\odot)$	$9.75^{+0.29}_{-0.38}$

Notes. [a] Only fluxes of emission lines detecting more than 2σ are shown. [b] Total flux of both lines in the doublet. [c] Time since the Big Bang. [d] Half-light radius along the semimajor axis. [e] Ratio between the semiminor and the semimajor axes.

F150W, F200W, F277W, F356W, and F444W filters with a Sérsic profile (Sérsic 1963). We used the Bayesian code PySersic (Pasha & Miller 2023)[5]. We inputted 5″×5″(42×42 kpc) images centered around AURORA-LQG1 and the point spread functions constructed for the DJA mosaics presented in Genin et al. (2025). Fitting was conducted individually and separately for each filter. The images, models, and residuals are shown in Appendix C.

Figure 3 shows the derived half-light semimajor radius and Sérsic index as a function of wavelength. The size at the 0.5 μm rest frame, covered by the F150W filter, is $0.41^{+0.03}_{-0.03}$ kpc. This value is significantly smaller than the average sizes of quiescent galaxies at the same stellar mass and redshift (e.g., $\sim$ 1.4 kpc according to the size-mass relation at $1.75 < z < 2.25$; Hamadouche et al. 2025), of more massive quiescent galaxies (median $\sim$ 0.9 kpc for $z \sim 2.5$ quiescent galaxies with $\log(M_\star/M_\odot) = 10.5$; Yang et al. 2025), and of star-forming galaxies with similar stellar mass (1.5 kpc; van der Wel et al. 2014; Yang et al. 2025). Considering the line ratio derived in Sect. 3.1, this compact size is not likely due to the significant contribution from a point-like AGN. Moreover, the sizes positively correlate with wavelength. Fitting a power law to the size as a function of rest-frame wavelength yields a positive gradient with a slope of $\gamma = \Delta \log r_{\rm eff} / \Delta \log \lambda_{\rm rest} = 0.12 \pm 0.05$, in contrast to the average trends recorded for more massive quiescent galaxies at the similar redshift, which show a negative correlation ($\gamma \sim -0.3$; van der Wel et al. 2014; Ito et al. 2024). At $z < 1$, size gradient strength correlates with stellar mass, with more pronounced positive size–wavelength trends observed at lower masses (Kawinwanichakij et al. 2021). The result for AURORA-LQG1 is consistent with these expectations, but at $z \sim 2$. This positive correlation implies that older stellar populations, traced by longer wavelengths, are more spatially extended than the younger one, assuming a negligible impact from spatial inhomogeneities in dust attenuation and metallicity. We estimate a Sérsic index of $n \sim 3$ across all filters, indicating that AURORA-LQG1 has a bulge-like spheroidal morphology. This value agrees with the median Sérsic index of quiescent galaxies with $\log(M_\star/M_\odot) > 10$ at $z \sim 2-3$ (e.g., van der Wel et al. 2012; Martorano et al. 2025). We return to the morphology of AURORA-LQG1 in Sect. 5.2.

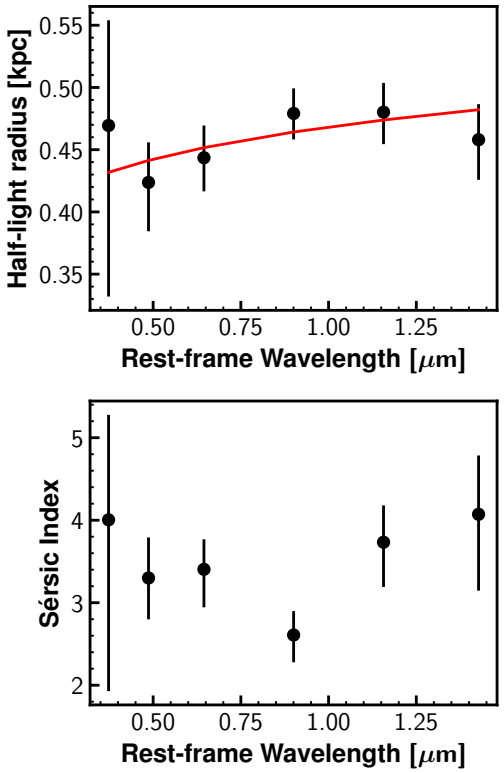

Fig. 3: Upper panel: Half-light radius as a function of the rest-frame wavelength. The red line corresponds to the best-fit power-law model. Bottom panel: Sérsic index as a function of the rest-frame wavelength.

4.2. Dynamical mass and constraints on the IMF

Combining the stellar velocity dispersion and morphological properties, we derived the dynamical mass of AURORA-LQG1

[5] https://github.com/pysersic/pysersic

as follows:

$$M_{\rm dyn} = \frac{\beta(n)\sigma_\star^2 r_{\rm eff}}{G}, \quad (1)$$

where n, $\sigma_\star$, $r_{\rm eff}$, and G are the Sérsic index, the stellar velocity dispersion, the effective radius, and the gravitational constant, respectively. We adopted the observed stellar velocity dispersion for $\sigma_\star$, but we note that the measured value may include a nonnegligible, yet unconstrained, contribution from rotational motion, as many massive quiescent galaxies at high redshift are reported to exhibit significant rotation (Toft et al. 2017; D'Eugenio et al. 2024; Slob et al. 2025). We employed the effective radius and Sérsic index measured in the F150W image, mapping the rest-frame optical wavelength, for consistency with the literature (Mendel et al. 2020; Stockmann et al. 2020; Forrest et al. 2022; Slob et al. 2025). The parameter β is a function of the Sérsic index, defined as $\beta(n) = 8.87 - 0.831\,n + 0.0241\,n^2$ (Cappellari et al. 2006). We note that the dynamical mass does not change significantly, even if we consider the homology correction based on the axis ratio proposed in van der Wel et al. (2022), due to a high axis ratio of AURORA-LQG1 ($q = 0.85^{+0.08}_{-0.06}$).

We estimate a dynamical mass of $\log(M_{\rm dyn}/M_\odot) = 9.75^{+0.29}_{-0.38}$. This estimate is among the lowest values reported for quiescent galaxies at $z \geq 1$ (Fig. 4), and it confirms the true low-mass nature of AURORA-LQG1. The comparison with the stellar mass estimate also allows us to place a first constraint on the IMF for quiescent galaxies in this stellar mass under the geometrical assumptions in Eq. 1. This is because the stellar mass depends on the assumption of the IMF, and the dynamical mass cannot be lower than the stellar mass. The dynamical-to-stellar mass ratio, assuming a Kroupa IMF (Sect. 3.2), is $\log(M_{\rm dyn}/M_\star) = 0.14^{+0.29}_{-0.38}$. Despite the large uncertainties, this value suggests that a more bottom-heavy, Salpeter (1955)-like IMF, yielding a 0.3 dex higher stellar mass, is disfavored. This is in line with studies at lower redshifts (e.g., Cappellari et al. 2013), which, based on different methods, show that the IMF of lower-mass galaxies is also less bottom-heavy.

4.3. Mass fundamental plane

In the local Universe, early-type galaxies follow a tight relation – known as the "fundamental plane" (Djorgovski & Davis 1987) – between their surface brightness, stellar velocity dispersion, and size. Swapping surface brightness for stellar mass surface brightness, the "mass" fundamental plane (MFP) was reported to be in place at cosmic noon for massive quiescent galaxies ($\log(M_\star/M_\odot) \sim 11$; Bezanson et al. 2013b). The MFP is independent of the evolution of stellar populations (Bezanson et al. 2013b), revealing the relationship between structural and morphological properties, and it has a negligible redshift evolution. Armed with the physical properties derived in the previous sections, we can test whether AURORA-LQG1 falls on the MFP. For consistency with the original definition of the MFP, we computed the circularized effective radius in F150W ($r_{\rm eff}\sqrt{q}$, where $q = 0.85^{+0.08}_{-0.06}$ is the projected axis ratio from the surface brightness modeling; Table 1). The stellar velocity dispersion is aperture-corrected to R_e by the correction function in Cappellari et al. (2006). Figure 5 shows that AURORA-LQG1 is consistent with an extension of the MFP toward lower masses at $z = 2$. This might hint at the fact that low-mass quiescent galaxies ($\log(M_\star/M_\odot) < 10$) also follow the same relation between dynamical properties and morphological properties of massive galaxies at $z = 0 - 2$. While archival NIRSpec spectra of massive quiescent galaxies can readily test the robustness MFP in the present epoch of JWST (Ito et al. 2025a, Ito et al. in prep.), lower-mass counterparts benefiting from deep medium resolution spectroscopy similar to AURORA-LQG1 are almost completely absent from public archives. It will thus be crucial to assemble statistical samples of quiescent galaxies with $\log(M_\star/M_\odot) < 10$ at cosmic noon to test our findings.

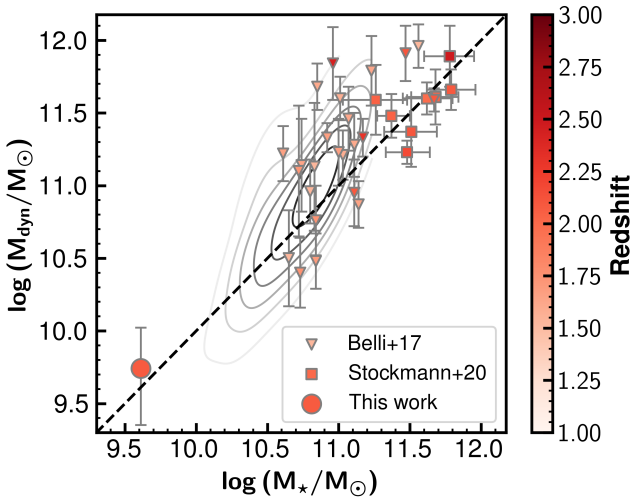

Fig. 4: Relation between stellar mass and dynamical mass for quiescent galaxies at $z = 2$. The large, filled circle marks the location of AURORA-LQG1. Dynamical mass estimates for quiescent galaxies at $1 < z < 3$ based on ground-based observations available in the literature are shown for comparison. The triangles and squares indicate the samples at $1.5 < z_{\rm spec} < 2.4$ from Belli et al. (2017) and $2 < z_{\rm spec} < 2.7$ from Stockmann et al. (2020), respectively. The symbols are color-coded according to redshift. The contours correspond to the distribution of dynamical mass and stellar mass for quiescent galaxies observed with JWST/NIRSpec and compiled in Ito et al. (2025a), measured in the same manner as AURORA-LQG1 (Ito et al., in prep.). The dashed black line represents the one-to-one relation.

5. Discussion

5.1. Formation history and downsizing in observations and simulations

At $z < 1$, stellar ages are known to correlate with stellar masses such that more massive systems are systematically older (i.e., they formed earlier) than less massive ones, an effect known as "downsizing" (e.g., Thomas et al. 2005, 2010; Gallazzi et al. 2005; Hamadouche et al. 2023; Gallazzi et al. 2025). We tested for a first possible hint of such an effect at $z \sim 2$ based on the SFH of AURORA-LQG1 and the archival sample of massive quiescent galaxies constrained by NIRSpec grating spectra in Ito et al. (2025a). For a fair comparison, we limited the redshift range to $1.9 < z < 2.3$ and the selection to quiescent galaxies that satisfy both the UVJ color selection and the sSFR selection as AURORA-LQG1 does. To constrain their SFHs, we modeled spectra and photometry with the same setup applied to AURORA-LQG1 (Sect. 3). After removing three sources where the modeling cannot constrain reliable quenching epochs, we re-

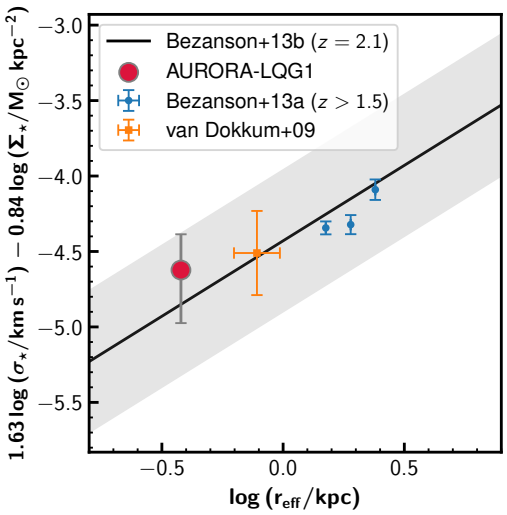

Fig. 5: Mass fundamental plane. The location of AURORA-LQG1 is marked by the red-filled circle, while data points for the quiescent galaxies at $z > 1.5$ from Bezanson et al. (2013a) and van Dokkum et al. (2009) are shown as blue circles and an orange square, respectively. The MFP at $z = 2$ from Bezanson et al. (2013b) is shown as a black line with a gray-shaded region indicating its 1σ uncertainty, derived from the 1σ uncertainty in the MFP parameters.

tained a sample of 15 quiescent galaxies with $M_\star > 10^{10}\,M_\odot$. Their best-fit spectra and photometry are shown in Appendix D.

Figure 6 shows the formation and quenching times of AURORA-LQG1 and the archival massive quiescent galaxies. To account for the slight redshift differences in the sample, we considered the time elapsed since the formation and quenching epoch ($t_{\mathrm{age}} - t_{\mathrm{form}}$, $t_{\mathrm{age}} - t_{\mathrm{quench}}$, where t_{age} is the age of the Universe at the observed redshift). The formation epoch of AURORA-LQG1 is similar to those of the massive sample. Overall, we do not observe a significant trend of downsizing in the current sample; the relatively high p-values from the Spearman rank correlation test ($\rho = 0.43$, $p = 0.1$) do not suggest a statistically significant correlation between $M_\star$ and $t_{\mathrm{age}} - t_{\mathrm{form}}$ across the 2 dex range of stellar masses shown in Fig. 6. In contrast, AURORA-LQG1 appears to be one of the most recently quenched galaxies in the sample at $z \sim 2$, making it more akin to "post-starburst" systems than the other massive quiescent galaxies. However, we do not find a statistically significant correlation between $M_\star$ and $t_{\mathrm{age}} - t_{\mathrm{quench}}$, with a Spearman rank correlation coefficient of $\rho = 0.46$ and a p-value of 0.07.

Next, we compared the SFH of AURORA-LQG1 with those of simulated quiescent galaxies. As an example, we used the Illustris TNG-100 simulation (Nelson et al. 2019). Quiescent galaxies in TNG-100 were selected as galaxies with sSFR $\leq 0.2/t_{\mathrm{age}}$. We note that all the observed massive quiescent galaxies in the literature compilation satisfy this criterion. The SFR used here is the average over 100 Myr, identical to the timescale adopted in the SED modeling with Bagpipes. Out of 500 subhalos hosting quiescent galaxies with $\log(M_\star/M_\odot) > 9$ at $z = 2.1$ (Snapshot ID=32), we find 38 galaxies in the mass range of AURORA-LQG1 ($9.5 < \log(M_\star/M_\odot) < 10$). We derived the SFH of each simulated galaxy from the distribution of the formation times of the stellar particles belonging to each subhalo at $z = 2.1$, sampled in bins of 10 Myr. The overall shape of the SFH of AURORA-LQG1 is in good agreement (within the 1σ uncertainty) with the median SFH of the simulated systems at $9.5 < \log(M_\star/M_\odot) < 10$. Moreover, we find that the formation and quenching epochs of AURORA-LQG1 are consistent with the distributions of those of the simulated quiescent galaxies in TNG-100 with similar masses and redshifts (Fig. 6). On the one hand, TNG-100 predicts a downsizing effect at $z = 2$, showing a weak but significant positive correlation between the stellar mass and the time since the formation epoch ($\rho = 0.25$ with $p < 0.01$ from a Spearman rank correlation test), i.e., more massive quiescent galaxies formed earlier. It does not predict a significant correlation ($\rho = -0.08$, with $p = 0.06$ from a Spearman rank correlation test) between the stellar mass and the time since the quenching epoch.

In summary, we find that the current JWST/NIRSpec grating spectroscopy sample of quiescent galaxies does not show a statistically significant downsizing signature at $z \sim 2$ (i.e., correlation between the stellar mass and formation time). The Illustris TNG-100 simulation predicts a star formation history of low-mass quiescent galaxies similar to that of AURORA-LQG1, but also a weak yet significant correlation between stellar mass and the formation time. Neither observation nor simulation predicts the significant correlation between the stellar mass and quenching time.

We note that such trends can vary among different simulations, as different simulations predict different star formation histories for high-redshift quiescent galaxies (Lagos et al. 2025). Figure 7 shows the distribution of quiescent galaxies in the TNG-100 simulation and the SHARK semi-analytical model (v2; Lagos et al. 2024). AURORA-LQG1 has values of look-back formation and quenching times consistent with those of systems with similar masses in SHARK. The look-back formation time of quiescent galaxies in SHARK is slightly higher than in TNG-100, whereas the distribution of the quenching time is similar. The dependency of the formation and quenching times on stellar mass is not clearly seen in the SHARK model, and the stellar mass distribution is different from that of TNG-100, as reported in Lagos et al. (2025). These discussions demonstrate that mass dependency of star formation history can be used to examine galaxy quenching in simulations. Again, it is critical to assemble a statistical sample of quiescent galaxies with $\log(M_\star/M_\odot) < 10$ to test different models for galaxy quenching robustly.

5.2. The connection with the surrounding overdense environment

AURORA-LQG1 is likely associated with a known rich protocluster at $z = 2.095$ extending over $\sim 3.7\times5$ pMpc^2 (Spitler et al. 2012; Yuan et al. 2014). However, AURORA-LQG1 does not fall at the spatial peak of the density map reported in the literature, and its redshift is slightly lower ($\Delta z \sim 0.01$, corresponding to $\sim 1000\,\mathrm{km\,s^{-1}}$) than the central redshift peak (Yuan et al. 2014).

To examine its local surrounding environment in detail, we investigated the presence of a possible localized overdensity. We first checked galaxies with photometric redshift estimates consistent with AURORA-LQG1's spectroscopic redshift ($z_{\mathrm{spec,LQG}}$) in the PRIMER-COSMOS catalog available on the DJA, based on eazy-py (Brammer et al. 2008) modeling of the photometry described in Sect. 2 (Valentino et al. 2023). We imposed cuts on the stellar mass at $\log(M_\star/M_\odot) > 8$, which is the stellar mass limit of the PRIMER-COSMOS catalog (Valentino et al. 2023), and on the redshift solutions defined as $|z_{\mathrm{phot,84}} - z_{\mathrm{phot,16}}|/z_{\mathrm{phot,50}} < 1$ to remove contaminants and poor fits, where $z_{\mathrm{phot,16}}$, $z_{\mathrm{phot,50}}$,

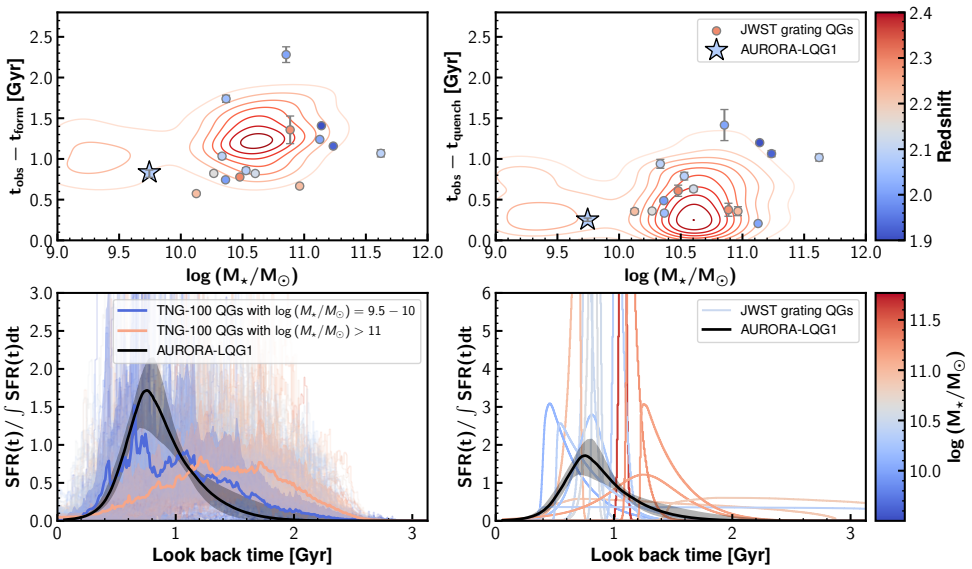

Fig. 6: Top row: Look-back formation ($t_{age} - t_{form}$, left panel) and quenching time ($t_{age} - t_{quench}$, right panel) as a function of stellar mass. In both panels, AURORA-LQG1 is marked with a star. The locations of 15 more massive quiescent galaxies at $z \sim 2$ with JWST/NIRSpec grating spectra from Ito et al. (2025a) are shown as colored circles. All symbols are color-coded according to their redshifts. The red contours indicate the distribution of quiescent galaxies in the Illustris TNG-100 simulation at $z = 2.1$. Bottom row: Normalized star formation histories of simulated quiescent galaxies in TNG-100 at $z = 2.1$ (left panel) and those of galaxies observed with NIRSpec grating spectroscopy compiled in Ito et al. (2025a). In the left panel, the median normalized SFHs of quiescent galaxies in TNG-100 with $9.5 < \log(M_\star/M_\odot) < 10$ and $\log(M_\star/M_\odot) > 11$ and their 16-84% percentiles are shown as thick blue and pink lines and shaded regions. In the right panel, the SFHs of the 15 quiescent galaxies used in the upper panels are color-coded according to their stellar masses.

$z_{phot,84}$ are the 16, 50, 84 percentiles of the probability distribution of the photometric redshift. The choice of the threshold for this criterion does not affect the following results. We then searched for galaxies with photometric redshifts $|z_{phot} - z_{spec,LQG}| < 0.1$, accounting for 1σ uncertainties on z_{phot}. We find six galaxies within 50 pkpc from AURORA-LQG1 that satisfy this selection. All of these are star-forming galaxies, and their stellar masses span a range between $\log(M_\star/M_\odot) = 8.2$ and 9.5, lower than our fiducial estimate for AURORA-LQG1. A search in the Keck/MOSFIRE archive[6], available as part of the ancillary data supporting the DJA, yields a tentative spectroscopic redshift for one of six sources with $\log(M_\star/M_\odot) \sim 9.5$, located ~ 20 pkpc from AURORA-LQG1. Its MOSFIRE K-band spectrum, reduced as described in Valentino et al. (2022), shows an emission line at $\lambda \sim 2.027\,\mu$m with a $S/N = 6$ (Fig. E.2 in Appendix E). Considering this galaxy's photometric redshift at $z \sim 2$, we conclude that the emission line is the Hα line, yielding a spectroscopic redshift of $z_{spec} = 2.0878 \pm 0.0002$.

To quantify the significance of the local overdensity around AURORA-LQG1, we computed the average number of galaxies within 50 pkpc around photometrically selected galaxies with similar stellar mass ($\log(M_\star/M_\odot) = 9.5 - 10$) at the same redshift ($1.98 < z < 2.18$). Surrounding galaxies with $\log(M_\star/M_\odot) > 8$ were selected around each central object as for AURORA-LQG1. For 345 galaxies with $\log(M_\star/M_\odot) = 9.5 - 10$ in the PRIMER-COSMOS catalog, we find an average of 2.1 ± 0.1 galaxies with $\log(M_\star/M_\odot) > 8$ within 50 pkpc. The presence of six companions around AURORA-LQG1 indicates that it resides in a region three times as dense as typical galaxies of similar mass. These results suggest that AURORA-LQG1 is not only part of a dense protocluster-scale structure but also a possibly locally overdense environment, although spectroscopic confirmation is required to robustly establish the group membership.

Recent studies on massive (Kubo et al. 2021; McConachie et al. 2022; Ito et al. 2023; Kakimoto et al. 2024; Ito et al. 2025b; McConachie et al. 2025; Sillassen et al. 2025) and low-mass (Sandles et al. 2023; Baker et al. 2026) quiescent galaxies at $z \geq 2$ also report that they reside in dense environments. Although it is difficult to conclude that such a dense environment is directly linked to the quenching of AURORA-LQG1, this is nonetheless in line with a possible connection between the quenching of low-mass quiescent galaxies and the environment, in principle.

Considering that our low-mass target AURORA-LQG1 was relatively rapidly quenched (< 1 Gyr), environmental processes such as tidal or ram-pressure stripping could potentially explain its properties. Furthermore, the positive size gradient with wavelength (Sect. 4.1) indicates that the older stellar populations are more spatially extended than the younger stars, suggesting an "outside-in" quenching scenario. This contrasts with massive quiescent galaxies, which are more commonly quenched "inside-out" (e.g., Cheng et al. 2025). We note that another low-mass quiescent galaxy at $z = 2$ in a dense environment (Sandles et al. 2023) exhibits a similar positive color gradient. Such outside-in quenching may be driven by the environmental effects described above. Additionally, dense environments foster frequent major and minor mergers, which could increase the size of AURORA-LQG1 at later epochs without significantly lowering its metallicity or altering its position on the MFP.

[6] https://grizli-cutout.herokuapp.com/mosfire?mode=table

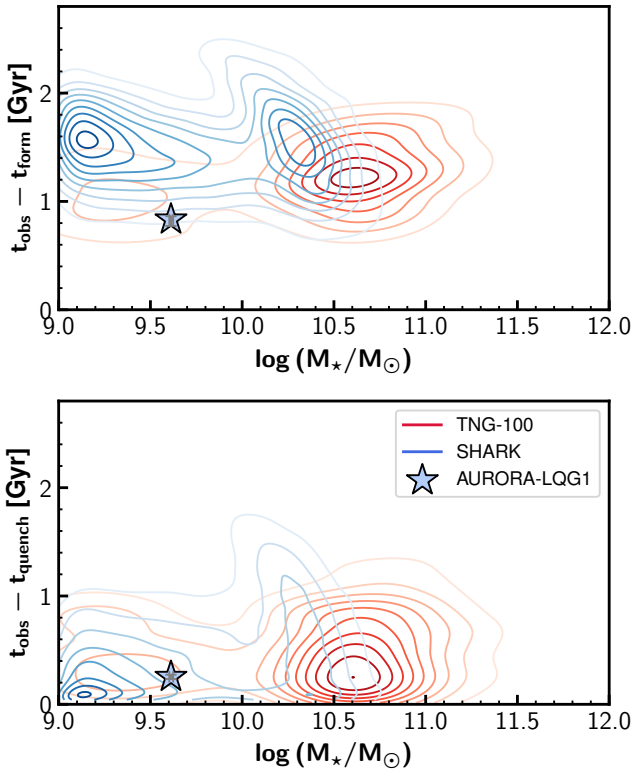

Fig. 7: Comparison of the distributions of look-back formation time ($t_{age} - t_{form}$, top panel) and quenching time ($t_{age} - t_{quench}$, bottom panel) as functions of stellar mass in TNG-100 (red contours) and SHARK (blue contours).

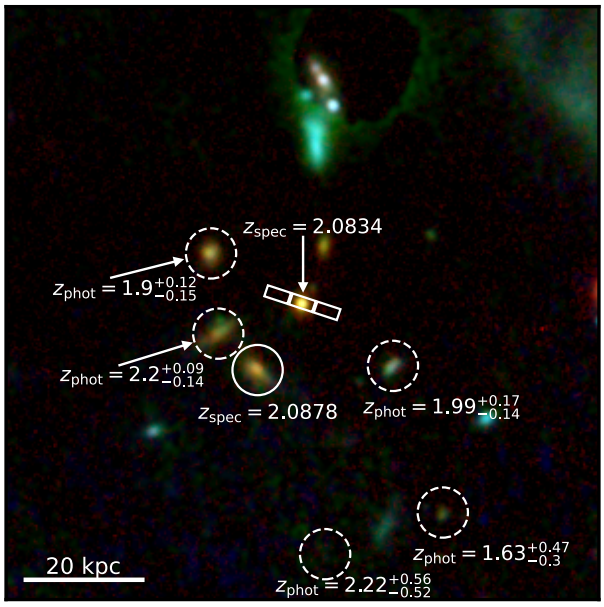

Fig. 8: 12″ × 12″ JWST/NIRCam composite image of AURORA-LQG1. Galaxies with spectroscopic (photometric) redshift estimates consistent with that of AURORA-LQG1 within their uncertainties are highlighted by solid (dashed) line circles. Their redshifts are also shown.

6. Summary

In this paper, we reported the spectroscopic confirmation of AURORA-LQG1, a low-mass quiescent galaxy at $z_{spec} = 2.0834$ with $\log(M_\star/M_\odot) = 9.6$. This galaxy lies ten times lower than the knee of the SMF of quiescent galaxies at $z = 2$, thus being one of the least massive quiescent galaxies at high redshifts observed with JWST/NIRSpec grating spectroscopy so far. Analyzing the deep medium-resolution spectra and photometry, we reach the following conclusions:

- Its stellar velocity dispersion is measured to be 95^{+38}_{-33} km s^{-1} from stellar template fitting. This value is lower than any other measurements reported for quiescent galaxies at $z \sim 2$, consistent with its low stellar mass.
- The spectro-photometric modeling returns a star formation history indicating that AURORA-LQG1 formed half of its stellar mass $\sim$ 1 Gyr before the time of observation, followed by quenching $\sim$ 0.2 Gyr prior to $z = 2.08$. This makes AURORA-LQG1 a bona fide quenched galaxy akin to more massive counterparts in the literature, unlike bluer systems in a temporary quiescent phase.
- Our multiwavelength morphological analysis indicates that AURORA-LQG1 is a compact ($r_{eff} = 0.41^{+0.03}_{-0.03}$ kpc in F150W) spheroid with a Sérsic of index $n = 3$ and a positive size gradient with wavelength, consistent with outside-in quenching.
- The combination of the low stellar velocity dispersion and compact size yields a dynamical mass of $\log(M_{dyn}/M_\odot) = 9.75^{+0.29}_{-0.38}$, which confirms the true low-mass nature of AURORA-LQG1.
- Under standard geometrical assumptions, the dynamical-to-stellar mass ratio ($\log(M_{dyn}/M_\star) = 0.14^{+0.40}_{-0.25}$) shows that a bottom-heavy Salpeter (1955) IMF is less preferable to the Kroupa (2001) IMF.
- AURORA-LQG1 is consistent with the MFP determined by massive quiescent galaxies with $M_\star \geq 10^{11}\,M_\odot$ at $z \sim 2$ (Bezanson et al. 2013b). This suggests a possible extension of the equilibrium regulating the structure and dynamics of massive quiescent galaxies at cosmic noon down masses 10–100× lower.
- Comparing the derived star formation history with those of massive quiescent galaxies, AURORA-LQG1 is among the most recently quenched systems at $z \sim 2$ observed with NIRSpec grating spectroscopy. However, we do not find a significant signature of downsizing, i.e., no statistically significant correlation between formation time and stellar mass. The star formation history of this galaxy is broadly consistent with those of quiescent galaxies of similar mass and redshift in the Illustris TNG-100 simulation and SHARK model.
- AURORA-LQG1 is surrounded by a possible, dense group-scale ($\sim$ 50 kpc) environment, containing five star-forming galaxies with $\log(M_\star/M_\odot) = 8.2 - 9.5$, consistent photometric redshifts, and one with a tentative spectroscopically confirmation. The galaxy is also part of a known larger protocluster-scale overdensity. This overdense environment may be linked to the properties and quenching of AURORA-LQG1, particularly the possible outside-in quenching scenario, as supported by the positive size gradient with wavelength.

This study shows that deep JWST/NIRSpec medium-resolution spectroscopy of low-mass quiescent galaxies at $z \geq 2$ provides access to a unique window on their physics. This enables unambiguous confirmation of their low-mass nature via dynamical analysis, robust reconstruction of star formation histories, and first constraints on critical quantities such as stellar

metallicities. The assembly of statistical samples is well within the reach of JWST/NIRSpec – as our study demonstrates – and represents the only way forward to obtain typical properties of quiescent galaxies as a function of mass and environment and to constrain the representative quenching mechanism in this low-stellar-mass range.

Acknowledgements. KI, FV, and PZ acknowledge support from the Independent Research Fund Denmark (DFF) under grant 3120-00043B. WMB would like to acknowledge support from DARK via the DARK Fellowship. This study was supported by JSPS KAKENHI Grant Numbers JP23K13141 and JP25K07361 and a research grant (VIL54489) from VILLUM FONDEN. This work is based on observations made with the NASA/ESA/CSA James Webb Space Telescope. The data were obtained from the Mikulski Archive for Space Telescopes at the Space Telescope Science Institute, which is operated by the Association of Universities for Research in Astronomy, Inc., under NASA contract NAS 5-03127 for JWST. These observations are associated with program #1914. Some of the data products presented herein were retrieved from the Dawn JWST Archive (DJA). DJA is an initiative of the Cosmic Dawn Center, which is funded by the Danish National Research Foundation under grant DNRF140.

References

Alberts, S., Williams, C. C., Helton, J. M., et al. 2024, ApJ, 975, 85
Antwi-Danso, J., Papovich, C., Esdaile, J., et al. 2025, ApJ, 978, 90
Baker, W. M., D'Eugenio, F., Maiolino, R., et al. 2025a, A&A, 697, A90
Baker, W. M., Ito, K., Valentino, F., et al. 2026, A&A, 706, A91
Baker, W. M., Lim, S., D'Eugenio, F., et al. 2025b, MNRAS, 539, 557
Baker, W. M., Valentino, F., Lagos, C. d. P., et al. 2025c, A&A, 702, A270
Balogh, M. L., Morris, S. L., Yee, H. K. C., Carlberg, R. G., & Ellingson, E. 1999, ApJ, 527, 54
Belli, S., Newman, A. B., & Ellis, R. S. 2017, ApJ, 834, 18
Belli, S., Newman, A. B., Ellis, R. S., & Konidaris, N. P. 2014, ApJ, 788, L29
Belli, S., Park, M., Davies, R. L., et al. 2024, Nature, 630, 54
Beverage, A. G., Kriek, M., Suess, K. A., et al. 2024, ApJ, 966, 234
Beverage, A. G., Slob, M., Kriek, M., et al. 2025, ApJ, 979, 249
Bezanson, R., van Dokkum, P., van de Sande, J., Franx, M., & Kriek, M. 2013a, ApJ, 764, L8
Bezanson, R., van Dokkum, P. G., van de Sande, J., et al. 2013b, ApJ, 779, L21
Brammer, G. 2023a, grizli
Brammer, G. 2023b, msaexp: NIRSpec analyis tools
Brammer, G. B., van Dokkum, P. G., & Coppi, P. 2008, ApJ, 686, 1503
Bressan, A., Marigo, P., Girardi, L., et al. 2012, MNRAS, 427, 127
Bruzual, G. & Charlot, S. 2003, MNRAS, 344, 1000
Calzetti, D., Armus, L., Bohlin, R. C., et al. 2000, ApJ, 533, 682
Cappellari, M. 2017, MNRAS, 466, 798
Cappellari, M. 2023, MNRAS, 526, 3273
Cappellari, M., Bacon, R., Bureau, M., et al. 2006, MNRAS, 366, 1126
Cappellari, M., McDermid, R. M., Alatalo, K., et al. 2013, MNRAS, 432, 1862
Carnall, A. C., Cullen, F., McLure, R. J., et al. 2024, MNRAS, 534, 325
Carnall, A. C., Leja, J., Johnson, B. D., et al. 2019a, ApJ, 873, 44
Carnall, A. C., McLure, R. J., Dunlop, J. S., et al. 2019b, MNRAS, 490, 417
Carnall, A. C., McLure, R. J., Dunlop, J. S., & Davé, R. 2018, MNRAS, 480, 4379
Carnall, A. C., McLure, R. J., Dunlop, J. S., et al. 2023, Nature, 619, 716
Cheng, C. M., Slob, M., Kriek, M., et al. 2025, arXiv e-prints, arXiv:2509.12316
Cimatti, A., Daddi, E., Renzini, A., et al. 2004, Nature, 430, 184
Conroy, C. & Gunn, J. E. 2010, ApJ, 712, 833
Cortese, L., Catinella, B., & Smith, R. 2021, PASA, 38, e035
Croton, D. J., Springel, V., White, S. D. M., et al. 2006, MNRAS, 365, 11
Cutler, S. E., Whitaker, K. E., Weaver, J. R., et al. 2024, ApJ, 967, L23
Davies, R. L., Belli, S., Park, M., et al. 2024, MNRAS, 528, 4976
de Graaff, A., Brammer, G., Weibel, A., et al. 2025a, A&A, 697, A189
de Graaff, A., Rix, H.-W., Carniani, S., et al. 2024, A&A, 684, A87
de Graaff, A., Setton, D. J., Brammer, G., et al. 2025b, Nature Astronomy, 9, 280
D'Eugenio, F., Pérez-González, P. G., Maiolino, R., et al. 2024, Nature Astronomy, 8, 1443
Djorgovski, S. & Davis, M. 1987, ApJ, 313, 59
Esdaile, J., Glazebrook, K., Labbé, I., et al. 2021, ApJ, 908, L35
Fabian, A. C. 2012, ARA&A, 50, 455
Falcón-Barroso, J., Sánchez-Blázquez, P., Vazdekis, A., et al. 2011, A&A, 532, A95
Forrest, B., Marsan, Z. C., Annunziatella, M., et al. 2020, ApJ, 903, 47
Forrest, B., Wilson, G., Muzzin, A., et al. 2022, ApJ, 938, 109
Gallazzi, A., Charlot, S., Brinchmann, J., White, S. D. M., & Tremonti, C. A. 2005, MNRAS, 362, 41
Gallazzi, A. R., Zibetti, S., van der Wel, A., et al. 2025, arXiv e-prints, arXiv:2511.11805
Genin, A., Shuntov, M., Brammer, G., et al. 2025, A&A, 699, A343
Glazebrook, K., Nanayakkara, T., Schreiber, C., et al. 2024, Nature, 628, 277
Glazebrook, K., Schreiber, C., Labbé, I., et al. 2017, Nature, 544, 71
Gunn, J. E. & Gott, III, J. R. 1972, ApJ, 176, 1
Hamadouche, M. L., Carnall, A. C., McLure, R. J., et al. 2023, MNRAS, 521, 5400
Hamadouche, M. L., McLure, R. J., Carnall, A. C., et al. 2025, MNRAS, 541, 463
Heintz, K. E., Brammer, G. B., Watson, D., et al. 2025, A&A, 693, A60
Horne, K. 1986, PASP, 98, 609
Ito, K., Tanaka, M., Valentino, F., et al. 2023, ApJ, 945, L9
Ito, K., Valentino, F., Brammer, G., et al. 2024, ApJ, 964, 192
Ito, K., Valentino, F., Brammer, G., et al. 2025a, arXiv e-prints, arXiv:2506.22642
Ito, K., Valentino, F., Farcy, M., et al. 2025b, A&A, 697, A111
Kakimoto, T., Tanaka, M., Onodera, M., et al. 2024, ApJ, 963, 49
Kawinwanichakij, L., Silverman, J. D., Ding, X., et al. 2021, ApJ, 921, 38
Kennicutt, R. C. & Evans, N. J. 2012, ARA&A, 50, 531
Kewley, L. J., Maier, C., Yabe, K., et al. 2013, ApJ, 774, L10
Kron, R. G. 1980, ApJS, 43, 305
Kroupa, P. 2001, MNRAS, 322, 231
Kubo, M., Umehata, H., Matsuda, Y., et al. 2021, ApJ, 919, 6
Lagos, C. d. P., Bravo, M., Tobar, R., et al. 2024, MNRAS, 531, 3551
Lagos, C. d. P., Valentino, F., Wright, R. J., et al. 2025, MNRAS, 536, 2324
Leja, J., Carnall, A. C., Johnson, B. D., Conroy, C., & Speagle, J. S. 2019, ApJ, 876, 3
Looser, T. J., D'Eugenio, F., Maiolino, R., et al. 2024, Nature, 629, 53
Marchesini, D., Brammer, G., Morishita, T., et al. 2023, ApJ, 942, L25
Martorano, M., van der Wel, A., Baes, M., et al. 2025, A&A, 694, A76
Mattolini, D., Zibetti, S., Gallazzi, A. R., Scholz-Díaz, L., & Pratesi, J. 2025, A&A, 703, A5
McConachie, I., Antwi-Danso, J., Chang, W., et al. 2025, arXiv e-prints, arXiv:2508.05752
McConachie, I., Wilson, G., Forrest, B., et al. 2022, ApJ, 926, 37
Mendel, J. T., Beifiori, A., Saglia, R. P., et al. 2020, ApJ, 899, 87
Nanayakkara, T., Glazebrook, K., Jacobs, C., et al. 2024, Scientific Reports, 14, 3724
Nanayakkara, T., Glazebrook, K., Kacprzak, G. G., et al. 2016, ApJ, 828, 21
Nanayakkara, T., Glazebrook, K., Schreiber, C., et al. 2025, ApJ, 981, 78
Nelson, D., Springel, V., Pillepich, A., et al. 2019, Computational Astrophysics and Cosmology, 6, 2
Oke, J. B. & Gunn, J. E. 1983, ApJ, 266, 713
Pacifici, C., Iyer, K. G., Mobasher, B., et al. 2023, ApJ, 944, 141
Park, M., Belli, S., Conroy, C., et al. 2024, ApJ, 976, 72
Pasha, I. & Miller, T. B. 2023, The Journal of Open Source Software, 8, 5703
Peng, Y., Maiolino, R., & Cochrane, R. 2015, Nature, 521, 192
Peng, Y.-j., Lilly, S. J., Kovač, K., et al. 2010, ApJ, 721, 193
Popesso, P., Concas, A., Cresci, G., et al. 2023, MNRAS, 519, 1526
Salpeter, E. E. 1955, ApJ, 121, 161
Sánchez-Blázquez, P., Peletier, R. F., Jiménez-Vicente, J., et al. 2006, MNRAS, 371, 703
Sandles, L., D'Eugenio, F., Helton, J. M., et al. 2023, arXiv e-prints, arXiv:2307.08633
Sato, R. A., Inoue, A. K., Harikane, Y., et al. 2024, MNRAS, 534, 3552
Scholz-Díaz, L., Martín-Navarro, I., & Falcón-Barroso, J. 2022, MNRAS, 511, 4900
Schreiber, C., Glazebrook, K., Nanayakkara, T., et al. 2018, A&A, 618, A85
Schreiber, C., Pannella, M., Elbaz, D., et al. 2015, A&A, 575, A74
Scoville, N., Aussel, H., Brusa, M., et al. 2007, ApJS, 172, 1
Sérsic, J. L. 1963, Boletin de la Asociacion Argentina de Astronomia La Plata Argentina, 6, 41
Shapley, A. E., Sanders, R. L., Topping, M. W., et al. 2025, ApJ, 980, 242
Shuntov, M., Ilbert, O., Lagos, C. d. P., et al. 2026, A&A, 707, A391
Sillassen, N. B., Jin, S., Magdis, G. E., et al. 2025, arXiv e-prints, arXiv:2510.23549
Slob, M., Kriek, M., Beverage, A. G., et al. 2024, ApJ, 973, 131
Slob, M., Kriek, M., de Graaff, A., et al. 2025, A&A, 702, A110
Spitler, L. R., Labbé, I., Glazebrook, K., et al. 2012, ApJ, 748, L21
Stockmann, M., Toft, S., Gallazzi, A., et al. 2020, ApJ, 888, 4
Strait, V., Brammer, G., Muzzin, A., et al. 2023, ApJ, 949, L23
Tanaka, M., Valentino, F., Toft, S., et al. 2019, ApJ, 885, L34
Thomas, D., Maraston, C., Bender, R., & Mendes de Oliveira, C. 2005, ApJ, 621, 673
Thomas, D., Maraston, C., Schawinski, K., Sarzi, M., & Silk, J. 2010, MNRAS, 404, 1775
Toft, S., Zabl, J., Richard, J., et al. 2017, Nature, 546, 510
Valentino, F., Brammer, G., Fujimoto, S., et al. 2022, ApJ, 929, L9
Valentino, F., Brammer, G., Gould, K. M. L., et al. 2023, ApJ, 947, 20
Valentino, F., Heintz, K. E., Brammer, G., et al. 2025, A&A, 699, A358
Valentino, F., Tanaka, M., Davidzon, I., et al. 2020, ApJ, 889, 93
van der Wel, A., Bell, E. F., Häussler, B., et al. 2012, ApJS, 203, 24
van der Wel, A., Franx, M., van Dokkum, P. G., et al. 2014, ApJ, 788, 28
van der Wel, A., van Houdt, J., Bezanson, R., et al. 2022, ApJ, 936, 9
van Dokkum, P. G., Kriek, M., & Franx, M. 2009, Nature, 460, 717
Weaver, J. R., Davidzon, I., Toft, S., et al. 2023, A&A, 677, A184
Weibel, A., de Graaff, A., Setton, D. J., et al. 2025, ApJ, 983, 11
Williams, R. J., Quadri, R. F., Franx, M., van Dokkum, P., & Labbé, I. 2009, ApJ, 691, 1879
Wu, P.-F. 2025, ApJ, 978, 131
Yang, L., Kartaltepe, J. S., Franco, M., et al. 2025, arXiv e-prints, arXiv:2504.07185
Yuan, T., Nanayakkara, T., Kacprzak, G. G., et al. 2014, ApJ, 795, L20

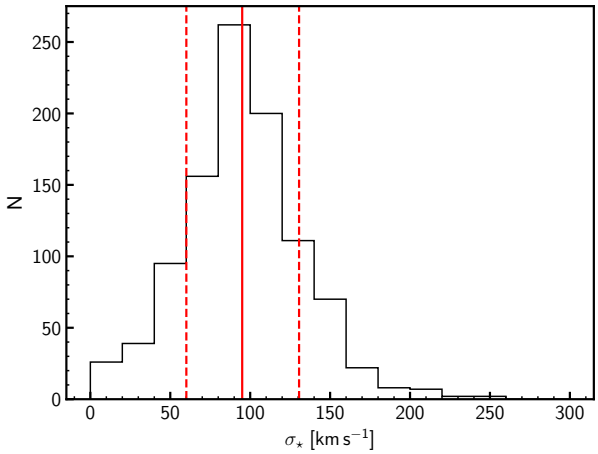

Fig. A.1: Probability distribution of the stellar velocity dispersion.

Table B.1: Free parameters and priors for the spectro-photometric modeling with Bagpipes .

Free parameter	Prior	Limits
$\sigma_\star$	Uniform	(10, 500)
$\log(M_{\rm formed}/M_\odot)$	Uniform	(1, 13)
A_V/mag	Uniform	(0, 4)
$Z/Z_\odot$	Logarithmic	(0.00355, 3.55)
a^a	Logarithmic	(0.1,10)
$P_0{}^b$	Gaussian ($\mu = 1, \sigma = 0.1$)	(0.75,1.25)
$P_1{}^b$	Gaussian ($\mu = 0, \sigma = 0.1$)	(-0.25,0.25)
$P_2{}^b$	Gaussian ($\mu = 0, \sigma = 0.1$)	(-0.25,0.25)
Parameters in the double-power-law SFH		
τ/Gyr	Uniform	(0.1, $t(z_{\rm obs})$)^c
α, β	Logarithmic	(10^{-2}, 10^3)
Parameters in the nonparametric SFH		
dsfr$_i$ (i=1,2,...,14)	Student-T	(-10, 10)

Notes. $^{(a)}$ White noise scaling factor. $^{(b)}$ Zero, first, and second-order polynomial correction function. $^{(c)}$ $t(z_{\rm obs})$ is the time since the Big Bang at the redshift of the sources.

Appendix A: Probability distribution of the stellar velocity dispersion

Figure A.1 shows the distribution of the stellar velocity dispersion obtained from the 1000 iterations of the ppxf fitting described in Sect. 3.1.

Appendix B: The configuration of the spectral-photometric modeling with Bagpipes

Table B.1 summarizes the free parameters and priors of the spectral photometric modeling with Bagpipes (Sect. 3.2).

Appendix C: Surface brightness fitting results

Figure C.1 shows the images, Sérsic models, and residuals in all NIRCam filters presented in Sect. 4.1.

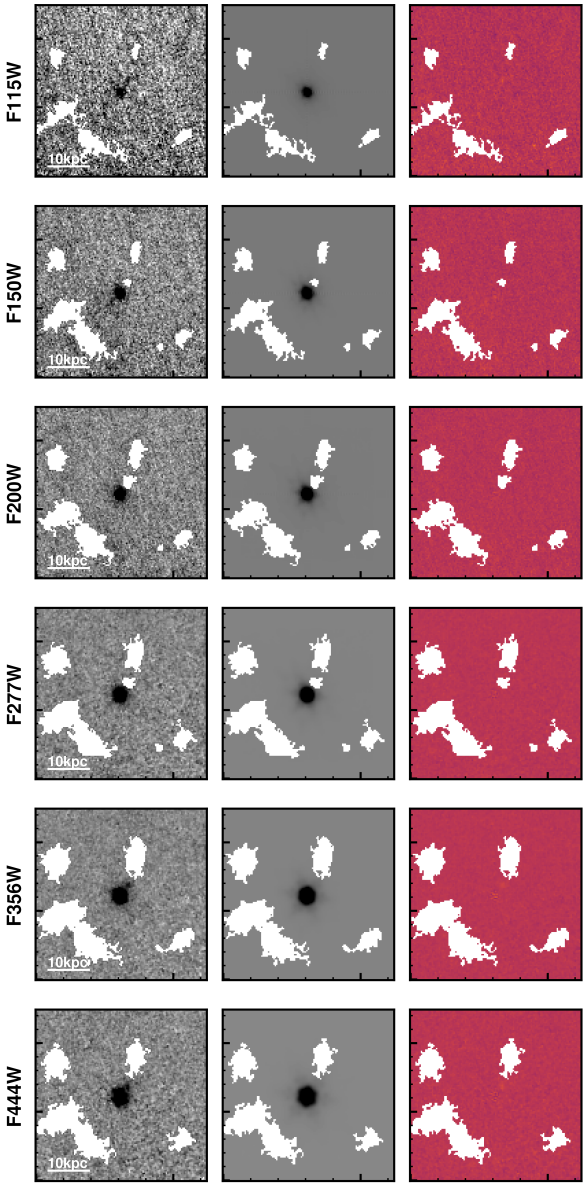

Fig. C.1: Surface brightness fitting results in the F115W, F150W, F200W, F277W, F356W, and F444W images (5.0″ × 5.0″). The observed images, model, and residuals are shown from left to right in each row. The white regions in each panel indicate masked nearby sources.

Appendix D: Spectro-photometric SED fitting for massive quiescent galaxies

Figure D.1 and Fig. D.2 show the spectra and photometry of massive quiescent galaxies used for comparison in terms of star formation history in Sect. 5.1. In these figures, the best-fit models from Bagpipes, which give us the estimates of their star formation histories, are also shown.

Appendix E: Galaxies around AURORA-LQG1

Figure E.1 shows the best-fit SED of six galaxies with photometric redshift consistent with that of AURORA-LQG1 and within a 50 pkpc radius (Sect. 5.2). Figure E.2 shows the Keck/MOSFIRE

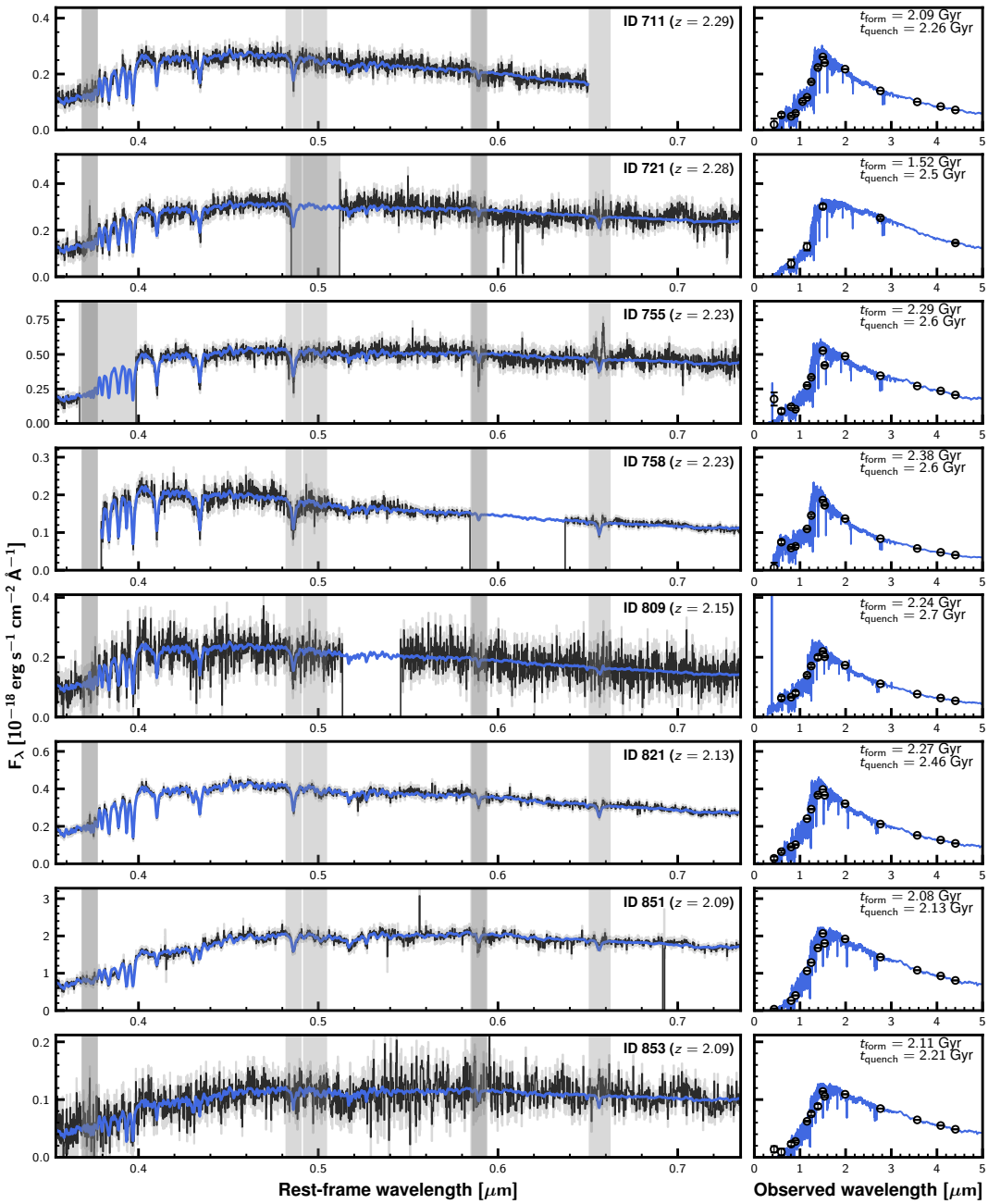

Fig. D.1: Left panels: JWST/NIRSpec spectra of massive quiescent galaxies used for comparison in Sect. 5.1. The black line and gray-shaded region correspond to the observed spectrum and its 1σ uncertainty, respectively. The blue line corresponds to the best-fit Bagpipes. The masked regions during the fitting and detector gaps are shown by the vertical gray rectangles. Right panels: Their photometric SEDs. The blue line is the best-fit SED obtained with Bagpipes.

K-band spectrum of one of these galaxies, showing a prominent emission line at $\lambda_{obs} \sim 2.027\,\mu$m detected at 6σ significance. This spectrum was taken as part of the ZFIRE survey (Nanayakkara et al. 2016). A Gaussian function is fitted to this emission line to derive the line center and total flux. Considering the redshift probability distribution function from eazy-py modeling, we conclude that the emission line corresponds to Hα, fixing the spectroscopic redshift to $z_{spec} = 2.0878 \pm 0.0002$.

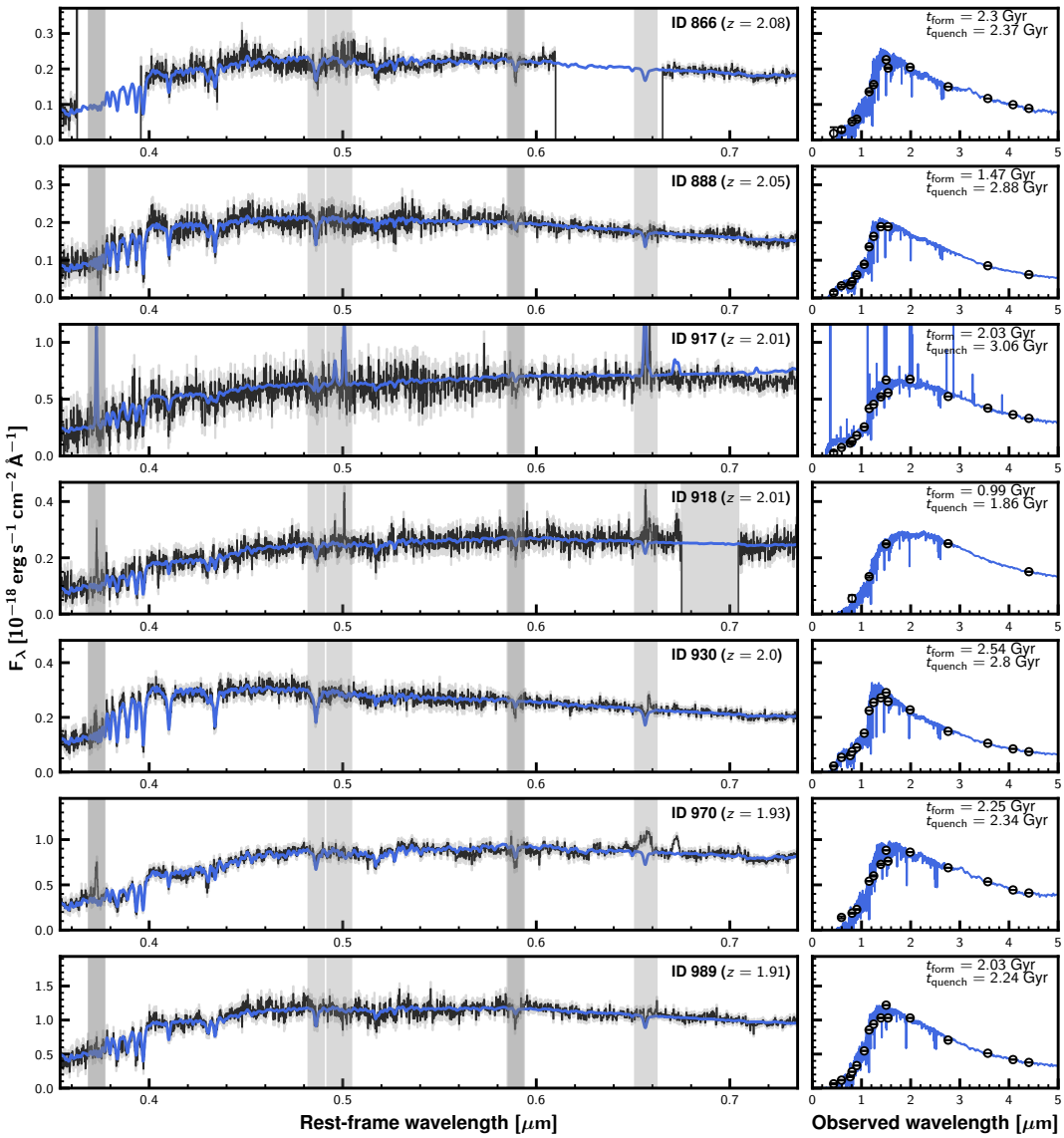

Fig. D.2: Continued.

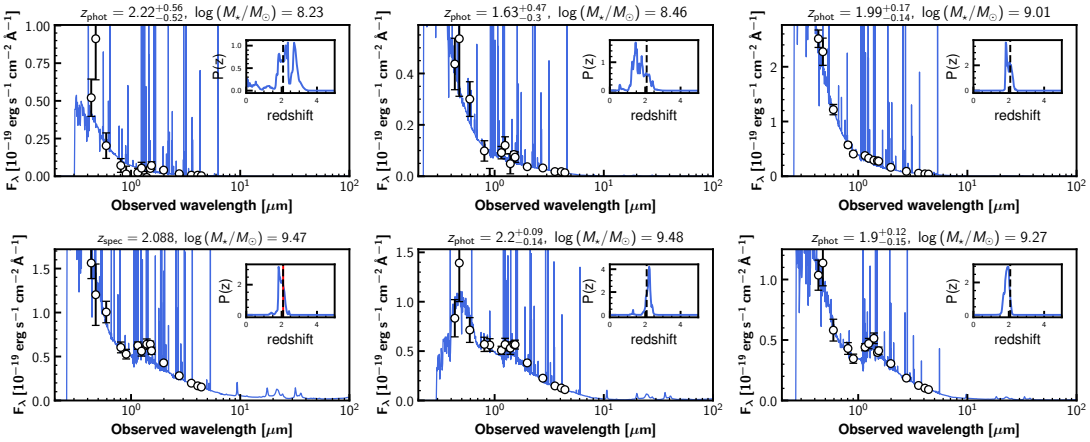

Fig. E.1: Best-fit SED of six galaxies within 50 pkpc from AURORA-LQG1 and with consistent redshifts. In each panel, the inset shows the probability distribution of their photometric redshift. The dashed black line corresponds to the spectroscopic redshift of AURORA-LQG1. One source at the lower left is spectroscopically confirmed, and its spectroscopic redshift is shown by the red line.

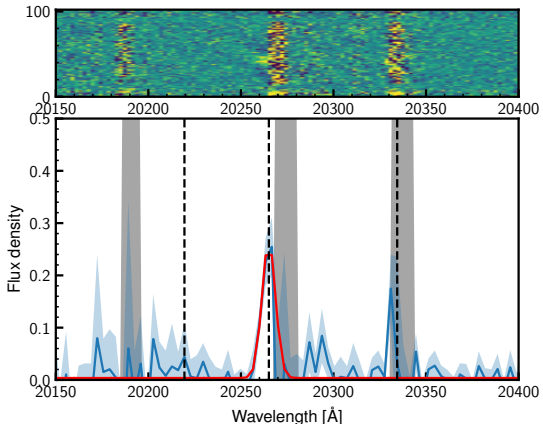

Fig. E.2: Keck/MOSFIRE K-band spectrum around an emission line in one of the galaxies close to the AURORA-LQG1. Top: 2D spectrum. Bottom: 1D extraction and its 1σ uncertainty in blue. The gray-shaded regions indicate wavelengths severely affected by sky lines. The best-fit Gaussian function used to determine the spectroscopic redshift is shown by the red line.